International Journal of Multiphase Flow 107 (2018) 131–145

Contents lists available at ScienceDirect

International Journal of Multiphase Flow

journal homepage: www.elsevier.com/locate/ijmulflow

Separation characteristics of the gas and liquid phases in a vane-type swirling flow field

Shuo Liu[a,b], Le-le Yang[a,b], Dong Zhang[a,b], Jing-yu Xu[a,b,*]

[a] Institute of Mechanics, Chinese Academy of Sciences, Beijing 100190, China
[b] School of Engineering Sciences, University of Chinese Academy of Sciences, Beijing 100049, China

ARTICLE INFO

Article history:
Received 14 January 2018
Revised 3 April 2018
Accepted 28 May 2018
Available online 5 June 2018

Keywords:
Gas–liquid separation
Bubble size distribution
Swirling flow field
Numerical simulation

ABSTRACT

In order to investigate inlet bubble size distribution, gas phase concentration, and swirling intensity in the swirling flow field of a vane-type separator, both flow loop experiments and numerical studies have been conducted in this work. The bubble size distributions and fractions of local voids were determined using a Malvern RTsizer and electrical resistance tomography, respectively, while the numerical simulations were conducted by coupling the RNG k-ε turbulent and mixture multiphase models. As a result, a suitable model for predicting the bubble size distribution parameters d_{32} and d_{max} was developed. In addition, the effects of inlet mixture flow rate, inlet void fraction, and liquid viscosity on the core size of the gas phase in the swirling flow field were determined, and the impact of the gas phase on swirling intensity was characterized using the swirling number. The obtained results can be used in designing vane-type separators for the crude oil extraction industry.

1. Introduction

In the petroleum industry, free gas is easily formed during the extraction of crude oil from wells that must be separated from the liquid phase for further processing. This operation is typically performed using vessel-type gas–liquid gravity settling separators whose workflow and design have been significantly improved during the last decades. However, the relatively high operational costs of these separators and the space limitations related to offshore petroleum extraction have led to the development of new separation methods. For this purpose, compact gas–liquid centrifugal separators represent the ideal choice. Their currently used industrial models include vertical annular separation and pumping systems, cyclone separators, and gas–liquid cylindrical cyclones (Hreiz et al., 2014). Among these systems, the cyclone separators utilize the concept of dispersion through a rapid swirling motion generated by a centrifuge that renders separation possible due to the density difference.

According to the literature, two different types of cyclone separators (tangent inlet and axial inlet ones) are used industrially (the latter are also called vane-type separators). The former type has been extensively studied and modified for several decades to make it compatible with various crude oil reservoirs and strict environmental standards, while the more recently developed axial inlet cyclone separators were initially designed as demisters for atomic fields (Cai et al., 2014). As compared to the tangential inlet cyclonic separators, the vane-type separators exhibit better separation efficiency and lower pressure drops during operation, and thus are more suitable at space-limiting conditions. To enhance the separation performance of vane-type separators, several research groups (Klujszo et al., 1999; Hoffman et al., 2006; Rafee et al., 2010; Shi and Xu, 2015; Cai et al., 2014) have investigated their designs and continuous phases at high inlet velocities both numerically and experimentally. Other researchers have focused on the gas–liquid two-phase flow. Funahashi et al. (2016) modeled the air-water two-phase swirling flow to examine the dependence of its characteristics and separator performance on the inlet liquid and gas fluxes. Wang et al. (2016) experimentally studied passive cyclonic gas–liquid separators using electrical capacitance volume tomography. Yin et al. (2017b) investigated the bubble trajectory inside an axial gas–liquid separator utilized for tritium removal from molten salt reactors through method of experiment study and found a correlation between the bubble size and separator performance.

To enhance the separation performance of these devices, it is important to determine the inlet bubble size distribution, gas phase concentration, and swirling intensity distribution in a swirling flow field. Unfortunately, none of these parameters has been previously investigated in sufficient detail. Hence, in this study, the bubble size distribution, gas phase distribution in a swirling flow field, and influence of the gas phase on the swirling

* Corresponding author at: Institute of Mechanics, Chinese Academy of Sciences, Bei-Si-Huan-Xi road No.15, Beijing 100190, China.
E-mail address: xujingyu@imech.ac.cn (J.-y. Xu).

https://doi.org/10.1016/j.ijmultiphaseflow.2018.05.025
0301-9322/

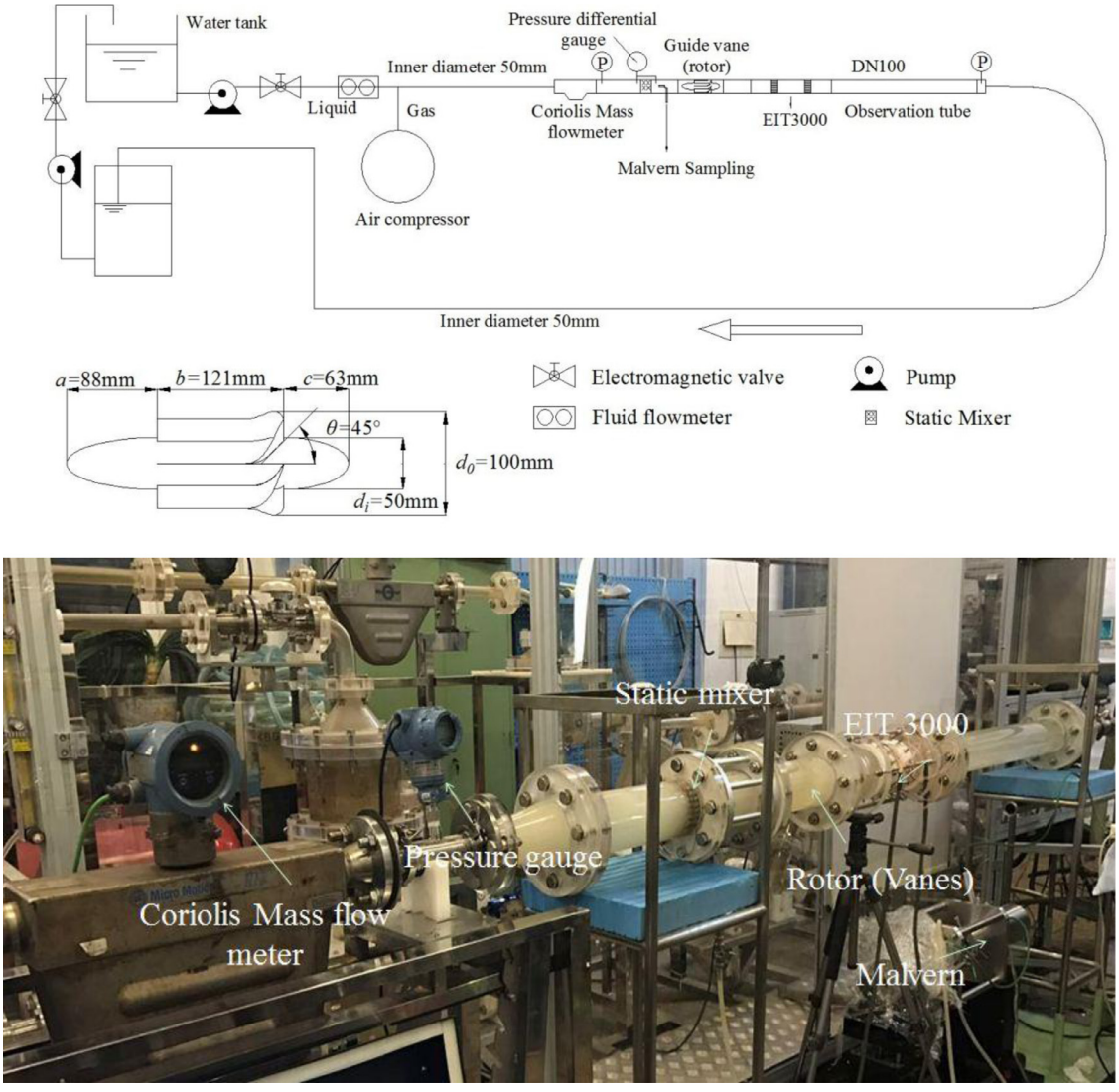

Fig. 1. Schematic and photo of the test facility.

intensity were examined to design a swirling vane-type separator with optimal characteristics for the petroleum industry. For this purpose, experimental studies and numerical simulations were conducted. In particular, the bubble size distribution and gas core sizes were determined using a Malvern RTsizer and electrical resistance tomography (ERT), respectively, while the numerical simulations were performed using the RNG k-ε turbulent and mixture multiphase models. Regularity of inlet bubble size distribution, gas phase distribution in the swirling flow field and influence of gas phase on the swirling intensity will be clarified.

2.1. Working fluids

In this work, tap water and carboxymethyl cellulose solution (CMC) are used as the working fluids. All the experiments are performed at a temperature of 20 °C, corresponding to a gas-water surface tension coefficient of 0.072 N·m.

2.2. Swirling guide vane configuration

A similar guide vane configuration is utilized for studying oil drop behavior in a swirling flow field (Liu et al., 2018). Six swirling vanes with a 0° inlet and 45° outlet angles have been fixed on the hub at equal 60° intervals. The vane thickness is 5 mm, while its other parameters are described in detail in Figs. 1and 2.

2.3. Measuring technique and systematic error

The focus of the experimental studies conducted in this work is to determine the bubble size distribution and local void fraction in a swirling flow field using the Malvern RTsizer and EIT 3000 instruments, respectively.

The Malvern RTsizer is an optical instrument containing a lens, a laser source, and detectors as the key elements. As is shown in Fig. 3, during measurements, bubbles pass through a scattered laser beam. At small forward angles, the scattering process is dominated by diffraction. Light passing through different sized bubbles have different angles. The scattered light is detected by a set of concentric annular detectors, indicating that each detector receives the light scattered at a specific angle independently of the bubble position. Thus, the bubble size distribution can be obtained either directly or through some mathematical transformations. Using the Mavlern RTsizer, the characteristic diameter distribution parameter d_{32} defined in Eq. (1) can be obtained together with the parameters d_{10}, d_{50}, and d_{90}, which are characteristic diameters that represent the highest droplets diameter of respectively 90%, 10% and 50% in volume of the dispersed phase. To determine

Fig. 2. Vane configuration.

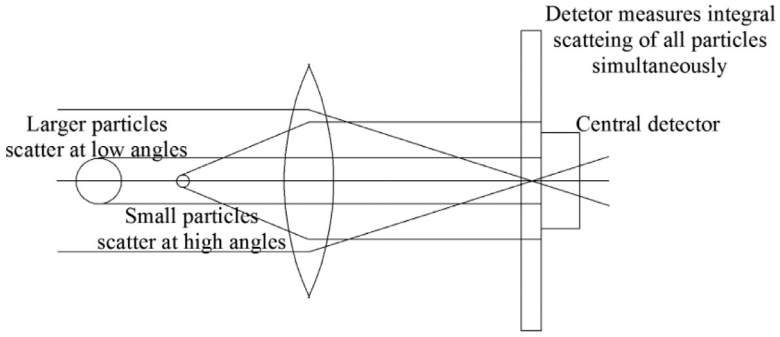

Fig. 3. Working principle of Malvern RTsizer.

the magnitude of the systematic error introduced by Malvern RTsizer, Hirleman et al. (1984) studied the response characteristics of a Malvern 2200 instrument both theoretically and experimentally. They found that the variations due to the combination of the detector calibration error and effects of a non-ideal lens corresponded to about 15% variation in the total instrument response. In this work, prior to conducting experiments the Malvern RTsizer was calibrated using a pure liquid without a gas phase, and the average deviation for all tests is less than 12.8%.

$$d_{32} = \frac{d_1^3 + d_2^3 + d_3^3 + \dots}{d_1^2 + d_2^2 + d_3^2 + \dots} \tag{1}$$

Furthermore, an EIT3000 instrument is used for measuring the local void fraction in a swirling flow field. It contains two electrodes with circular shapes (named section I and section II), which are placed at positions 5.6*D* and 7.2*D* downstream of the guide vanes corresponding to the developing and stable regions of the swirling flow field, respectively. In each plane, sixteen stainless steel electrodes are mounted around the pipe wall at equal intervals. The local void fraction is determined using the Maxwell equations. The concentration profile obtained using ERT can be erroneous to some degree due to the variety of reasons, such as the accuracy of the electrical measurements conducted at the system boundary and utilized image reconstruction algorithm. For example, the reference measurement error of 1% can lead to a conductivity error of up to 10% depending on the charge magnitude (Wang et al., 1999). Thus, prior to collecting data, the ERT instrument has been calibrated by filling the sensor with a liquid; as a result, the reference measurement error does not exceed 1%.

2.4. Experimental design

The swirling vane, measurement equipment, and observational components are assembled along the flow loop, as shown in Fig. 1. The rotator and turbine flow meters are used upstream of the testing section to measure the flow rates of the gas and liquid before mixing, respectively. The gas is injected into the water and flows through the static mixture to create a dispersion. In the test section, a Coriolis mass flowmeter is utilized to determine the density and flow rate of the mixture. Two pressure gauges are attached next to the Coriolis mass flowmeter and at the end of the test section to monitor the pressure drop inside the tube. The sampling equipment with movable elbows is connected to the Malvern RTsizer and before the swirling vane to determine the inlet bubble size distribution. The double pixels of the EIT instrument are mounted at a distance from the vane zone. A one-meter long horizontal tube is attached downstream for conducting visual observations and taking photographs. The entire testing section is fabricated from Plexiglass with an inner diameter of 100 mm.

2.5. Data matrix

All experiments are conducted at six liquid flow rates ranging from 8 m^3/h to 18 m^3/h at 2 m^3/h intervals and 10 gas flow rates ranging from 0 to 45 L/min at 5 L/min intervals. The liquid flow rate is confirmed when the gas flow rate gradually increases from 0 until no air bubbles are visible in the observational tube. The same method is used for the gas-CMC solution dispersion experiments with different inlet liquid flow rates. In particular, two mixture flow rates, 16 m^3/h and 18 m^3/h, are used for the gas-CMC solutions, while the CMC concentrations are equal to 200 mg/L, 1000 mg/L, and 2000 mg/L.

The resulting 68 combinations of experimental parameters are summarized in a single data matrix. The dataset for each case includes the gauge pressure, flow rate, density, bubble size distribution parameters (d_{10}, d_{50}, d_{90}, and d_{32}), and results of EIT measurements. In order to minimize the measurement error, each experiment has been repeated several times.

3. Numerical simulations

3.1. Modeling procedure

3.1.1. Multiphase model selection

In the present study, the gas phase forms continuous gas core in the whole swirling flow field, as shown in Fig. 4. The phenomenon is obviously phase segregated. For multiphase flows where the phases segregate totally, the mixture model can be further simplified into the volume of fluid model (VOF). Brennan (2016) adopted

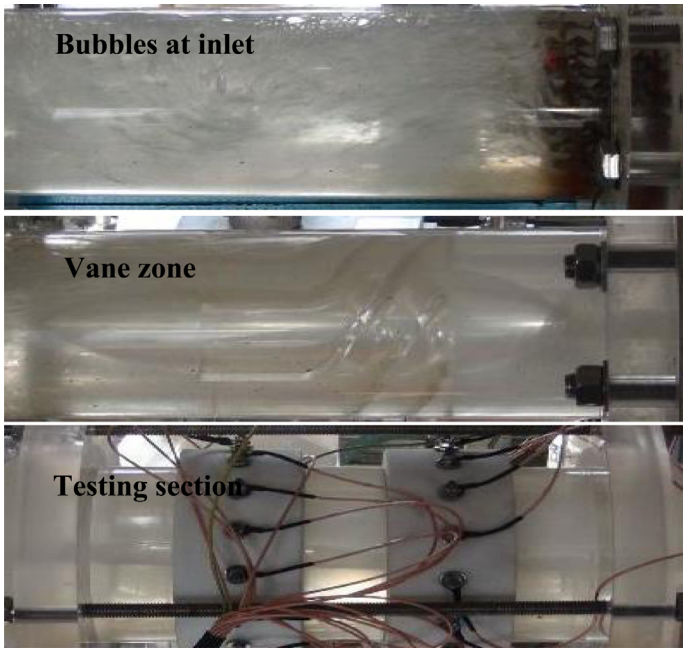

Fig. 4. Gas phase distribution in the swirling flow field.

the VOF and mixture models to simulate air core. Through comparison with experimental data, they found that the velocity predictions using the VOF and the mixture models were essentially the same. Yin et al. (2017a) pointed out that VOF and mixture model took the advantages in that the macro flow variables, such as the pressure or velocity profile could be predicted with acceptable accuracy for segregated flow, but for small bubbles, effects of various interface forces like the drag force, the shear-induced lift force, the virtual mass force on the bubble behavior could not be investigated. It can be seen from works above that mixture turbulent model is enough and the interface force can be neglected in the continuous gas core with reasonable accuracy. As a consequence, in this work, due to the continuous gas core, mixture multiphase model was applied. What's more, gas core configuration was similar as that done by Yin et al. (2017a). According to the reference above, we chose mixture as multiphase model and neglect interfacial force due to the continuous gas core in the swirling flow field.

The continuity equation for the mixture is

$$\frac{\partial}{\partial t}(\rho_m) + \nabla \cdot (\rho_m \vec{v}_m) = \dot{m} \tag{2}$$

where ρ_m is the mixture density, $\vec{v}_m$ is the mass-averaged velocity, and $\dot{m}$ is the user-defined transfer of the mass source. The variables $\vec{v}_m$ and ρ_m can be defined through the following equations:

$$\vec{v_m} = \frac{\sum_{k=1}^{n} \alpha_k \rho_k \vec{v}_m}{\rho_m} \tag{3}$$

$$\rho_m = \sum_{k=1}^{n} \alpha_k \rho_k \tag{4}$$

where $\vec{v}_k$ and α_k are the velocity and volume fraction of the kth phase, respectively.

The momentum equation is expressed as follows:

$$\begin{aligned}\frac{\partial}{\partial t}(\rho_m \vec{v}_m) + \nabla \cdot (\rho_m \vec{v}_m \vec{v}_m) \\ = -\nabla P + \nabla \cdot \left[\mu_m \left(\nabla \vec{v}_m + \nabla \vec{v}_m^T\right)\right] \\ + \rho_m \vec{g} + \vec{F} + \nabla \cdot \left(\sum_{k=1}^{n} \alpha_k \rho_k \vec{v}_{dr,k} \vec{v}_{dr,k}\right)\end{aligned} \tag{5}$$

where n is the number of phases, $\vec{F}$ is the body force, μ_m is the mixture viscosity, and $\vec{v_{dr,k}}$ is the drift velocity of the kth phase. The variables $\vec{v}_{dr,k}$ and μ_m can be obtained according to the following equations:

$$\mu_m = \sum_{k=1}^{n} \alpha_k \mu_k \tag{6}$$

$$\vec{v}_{dr,k} = \vec{v}_k - \vec{v}_m \tag{7}$$

In addition, the energy equation for the mixture model is defined as:

$$\begin{aligned}\frac{\partial}{\partial t} \sum_{k=1}^{n} (\alpha_k \rho_k E_k) + \nabla \sum_{k=1}^{n} \left(\alpha_k \vec{v}_k (\rho_k E_k + p)\right) \\ = \nabla \cdot \left(k_{eff} \nabla T\right) + S_E\end{aligned} \tag{8}$$

where k_{eff} is the effective conductivity ($\Sigma \alpha_k (k_k + k_t)$), and k_t is the turbulent thermal conductivity defined according to the utilized turbulence model. The parameter S_E takes into account other volumetric heat sources.

$$E_k = h_k - \frac{p}{\rho_k} + \frac{v_k^2}{2} \tag{9}$$

3.1.2. Turbulent model selection

Though RSM model has better performance generally due to its anisotropic hypothesis and accounts for the effects of streamline curvature, swirling, rotation and rapid changes in strain rate, the fidelity of RSM prediction is still limited by the closure assumptions such as modeling of the pressure-strain and dissipation-rate terms. Thus, RSM model is not always performs well in all the cases. For instance, Saidi et al. (2013) found that the RSM predicted both qualitatively and quantitatively inaccurate tangential velocity profiles.

RNG k-ε can account for effects of swirl or rotation by modifying the turbulent viscosity appropriately. Jawarneh et al. (2008) numerically studied a swirling two-phase flow in a cylindrical separator with double vertex generators to predict the separation efficiency of oil and sand using the RNG k-ε turbulent model. The obtained results were in a good agreement with the experimental data in terms of the mean tangential velocity and mean pressure profile. Javadi et al. (2016) conducted the experimental and numerical investigations of the unsteadiness generated in a swirl apparatus using the RNG k-ε turbulent model and demonstrated its suitability for predicting the mean flow velocity. Escue and Cui (2010) compared tangential velocity profiles obtained from experiments with results from numerical simulation from both RNG k-ε model and RSM model for swirling pipe flows, which had similar structure in this work. The results showed that RNG k-ε had better performance in cases of swirling number less than 2.0.

On the basis of works above, a comparison between RSM and RNG k-ε turbulent model at 2D downstream vane zone was carried out under inlet water flow rate 18.0 m^3/h. It can be seen in Fig. 5 that radical distribution of velocity and pressure are nearly the same for the two turbulent models. What's more, through comparison of phase distribution listed in Fig. 6, RSM model is unable to predict proper gas core in the swirling flow field while RNG k-ε turbulent model give a proper gas phase distribution as experimental observation. This is probably due to the fact that swirling flow field induced by guide vane is a relatively weak one and the influence of anisotropic is not so prominent compared to that of a traditional conical hydrocyclone.

In the present study, the maximal swirling number in the swirling flow field is less than 2.0, as shown in Fig. 27, which is in coincident with research work done by Escue and Cui (2010); Besides, performance of continuous phase prediction is nearly the

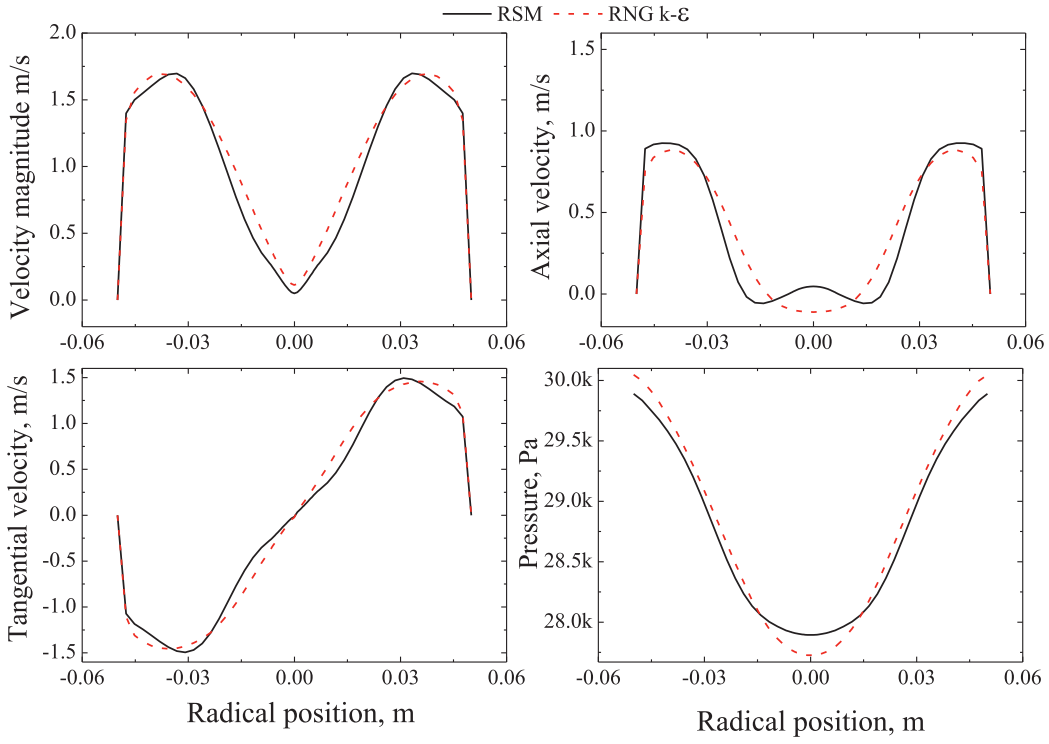

Fig. 5. Comparison between RSM and RNG k-ε turbulent model at 2D downstream vane zone.

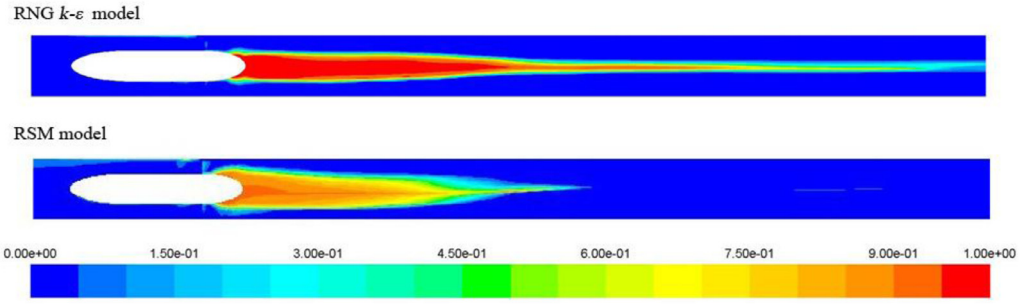

Fig. 6. Comparison between phase distributions of two turbulent model.

same for RNG k-ε and RSM under this condition. Thus, RNG k-ε model is applied in this work.

The transport equations of the RNG k-ε turbulent model are defined as follows:

$$\frac{\partial}{\partial t}(\rho k)+\frac{\partial}{\partial x_j}(\rho k u_i)=\frac{\partial}{\partial x_j}\left(\alpha_k \mu_{eff}\frac{\partial k}{\partial x_j}\right)+G_k+G_b-\rho\zeta-Y_M+S_K \tag{10}$$

$$\frac{\partial}{\partial t}(\rho \zeta)+\frac{\partial}{\partial x_j}(\rho \zeta u_i)=\frac{\partial}{\partial x_j}\left(\alpha_\zeta \mu_{eff}\frac{\partial \zeta}{\partial x_j}\right)+G_{1\zeta}\frac{\zeta}{k}\left(G_k+G_{3\zeta}G_b\right) -G_{2\zeta}\rho\frac{\zeta^2}{k}-R_\zeta+S_\zeta \tag{11}$$

here, the term G_k represents the turbulence kinetic energy generated due to the existence of mean velocity gradients. G_b is the turbulence kinetic energy generated due to buoyancy. Y_M represents the contribution of the fluctuating dilatation in compressible turbulence to the overall dissipation rate. The parameters k and ζ correspond to the inverse effective Prandtl numbers. S_k and S_ζ are the user-defined source terms. In addition, proper modification of the turbulent viscosity can make the RNG k-ε model suitable for describing swirling or rotation motions as well.

3.2. Geometry and boundary conditions

The three-dimensional geometric model of the fluid domain is constructed using the ANSYS Workbench software. The fluid domain represents a 2.6 m long cylindrical model with a hollow vane hub and vane zone sliced by area similar to vane shape. The grid is created using the ANSYS ICEM CFD software package.

The computational domain is occupied by the two-phase flow, in which the liquid corresponds to the continuous phase and the gas represents the dispersed phase. Here, the inlet bubble size is determined from the results of experimental measurements performed using the Malvern RTsizer as shown in Fig. 7. As a boundary condition, the inlet is defined as an inlet with a velocity vector perpendicular to the face (the velocities of the gas phase and liquid phase are defined respectively). The inlet void fraction ε is calculated from the inlet mixture density measured by the Coriolis mass flowmeter. The hydraulic diameter is set to 0.1 m, which is equal to the pipe inner diameter. The pressure at the outlet of the fluid domain is equal to the experimentally measured value under experimental conditions. For conditions with high inlet flow rates (larger

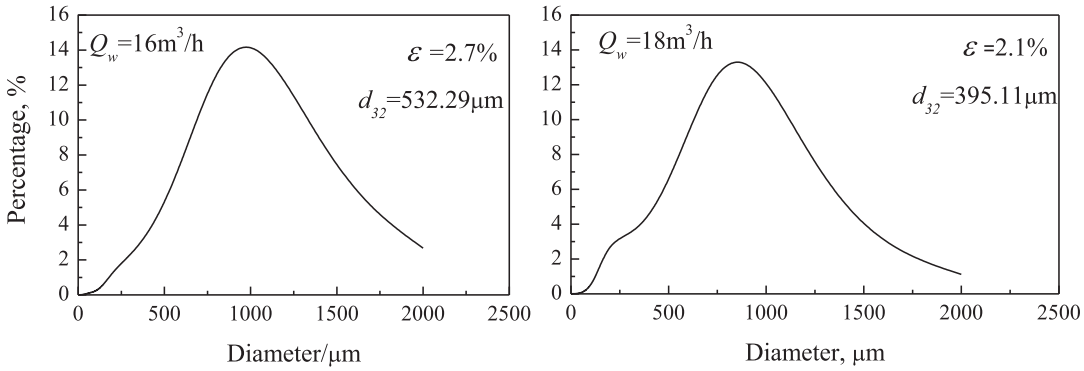

Fig. 7. Inlet bubble size distribution for 16 m^3/h and 18 m^3/h water inlet flow rates respectively.

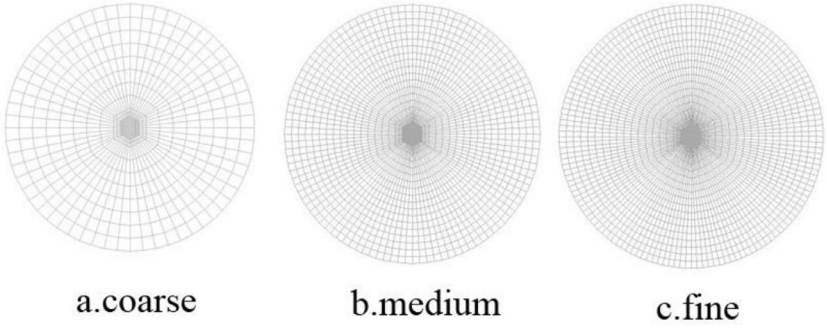

Fig. 8. Grid configuration for different qualities (a. coarse, b. medium, c. fine).

than 56 m^3/h), outflow are applied with center of vane zone inlet as reference location. The pipe walls, hub, and vanes represent the no-slip boundary conditions.

3.3. Solution method

In the experimental studies, the inlet flow rates range from 8 m^3/h to 18 m^3/h, whose Reynolds numbers ranging between 28,300 and 63,700 correspond to the turbulent region. In numerical simulations, the RNG k-ε model was utilized as the turbulent model, while the mixture model was used as the multiphase model.

Considering the unsteadiness of the bubble dispersion flow, the numerical simulations are conducted in an unsteady mode characterized by a time step of 50 ms. A semi-implicit method for pressure-linked equation is utilized to couple the pressure and velocity. Pressure spatial discretization is defined as PRESTO, while momentum, volume fraction, turbulent kinetic energy spatial discretization are defined in the second-order upwind form. Time discretization is performed using an implicit first-order procedure. The residual scales in all simulations are set to 10^{-5}.

3.4. Grid-independent studies

A mesh-independent study, whose boundary conditions correspond to the facial average static pressure, inlet velocity of 0.637 m/s, and pressure at the outlet equal to 39 kPa has been conducted before the numerical simulations. During this procedure, grid refinement is performed axially, peripherally, and radially (see Fig. 8 describing three different levels of the grid quality). Fig. 8(a) displays a relatively coarse grid containing 106,880 cells; Fig. 8(b) shows a relatively medium grid with 665,280 cells; and Fig. 8(c) depicts a relatively fine grid with 1,283,904 cells. Fig. 9 shows the variations of the average face static pressure and axial velocity with the grid quality, indicating that the change from c to b is much smaller than that from b to a. Thus, the average relative changes in the static pressure and velocity magnitude from b to a are 0.17% and 5.7%, while the values obtained after changing the grid from c to b are equal to 0.14% and 2.6%, respectively. Hence, grid b containing 665,280 cells can be considered sufficiently fine to satisfy the grid independence requirements, and all further numerical studies are conducted using scheme b.

4. Results and discussion

4.1. Bubble size distribution

Before examining the regularity of the swirling flow field, the bubble size distribution in the upstream vane zone is first studied experimentally. As the gas-water mixture flows through the static mixture and is immediately turned into dispersed bubbles, the bubble size distribution characterized by the parameters d_{max} and d_{32} can be recorded by Malvern RTsizer. On the other hand, the turbulent energy dissipation ζ can be calculated using the following equation:

$$\zeta = \left(\frac{\Delta P}{L}\right)_{sm} \frac{u_m}{\alpha_m \rho_m} \tag{12}$$

where ΔP is the pressure drop of the static mixture obtained from pressure differential gauge of Fig. 1; L is the length of the static mixture; u_m and ρ_m are the velocity and density of the gas–liquid dispersion, respectively; and α_m is the porosity of the static mixture.

The plots of d_{max} as a function of the turbulent energy dissipation ζ are shown in Fig. 10. In this figure, the data obtained for both the gas-water dispersion and gas-CMC dispersion are presented. The scattered dots represent the experimental data, while the solid lines are generated using the prediction model developed

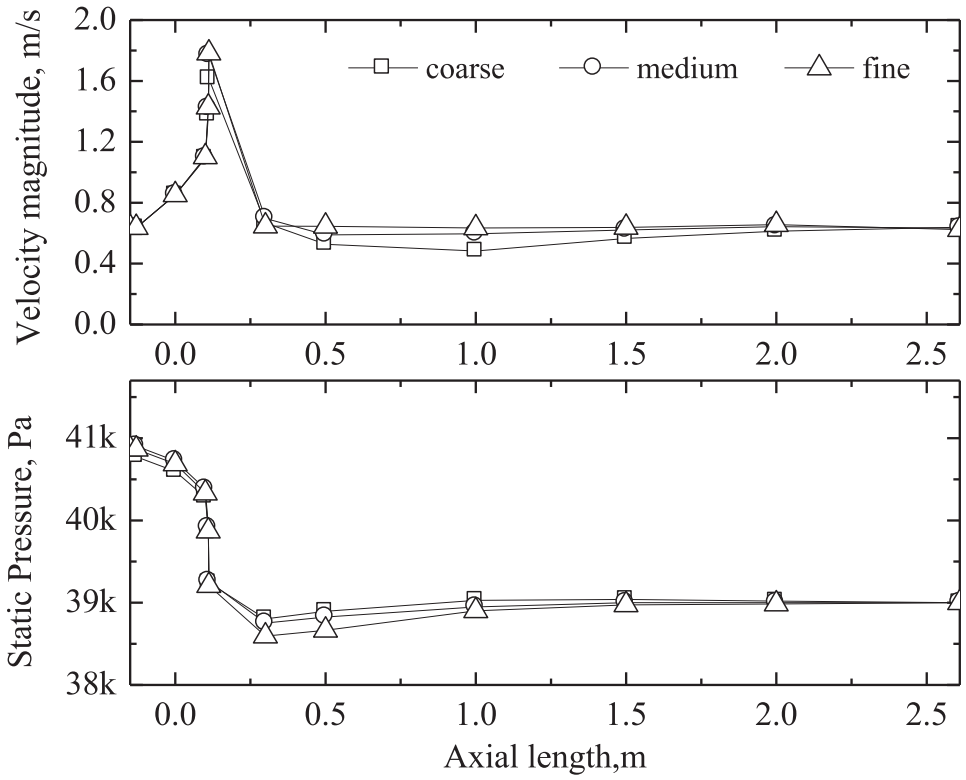

Fig. 9. Comparison of section average velocity magnitude and static pressure for different grid density (a. coarse, b. medium, c. fine).

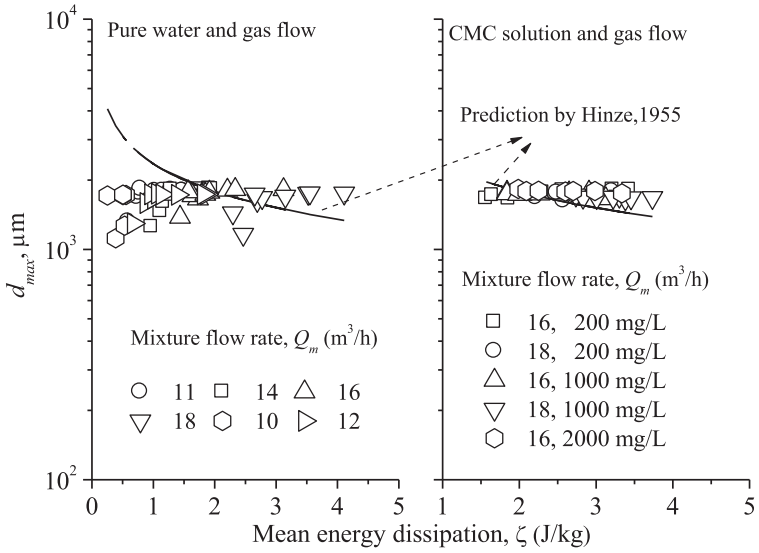

Fig. 10. Comparison between experimental data (symbols) and theoretical model (continuous line) for dmax vs. mean energy dissipation.

by Hinze (1955):

$$\frac{d_{\max}}{D} = 0.55\left(\frac{\rho_c u_c^2 D}{\sigma}\right)^{-0.6} f^{-0.4} \tag{13}$$

where u_c is the velocity of the continuous phase, ρ_c is the density of the continuous phase, σ is the interfacial tension, and D is the pipe diameter. The friction factor of the static mixture f can be calculated through Eq. (14), in which the parameter D_h represents its hydraulic diameter:

$$f = \left(\frac{\Delta P}{L}\right)_{sm} \frac{\alpha^2 D_h}{2u_m^2 \rho_m} \tag{14}$$

Hinze's model is able to predict the maximal drop size in dispersions and has been enhanced by many researchers for several decades. In this work, it is modified using Eq. (15), which assumes a scale factor of 0.6 for the constant 0.55 in Eq. (13) in order to better match the experimental values of d_{max} measured at the specified conditions. As shown in Fig. (10), the modified model fits experimental data relatively well for both the pure water-gas and

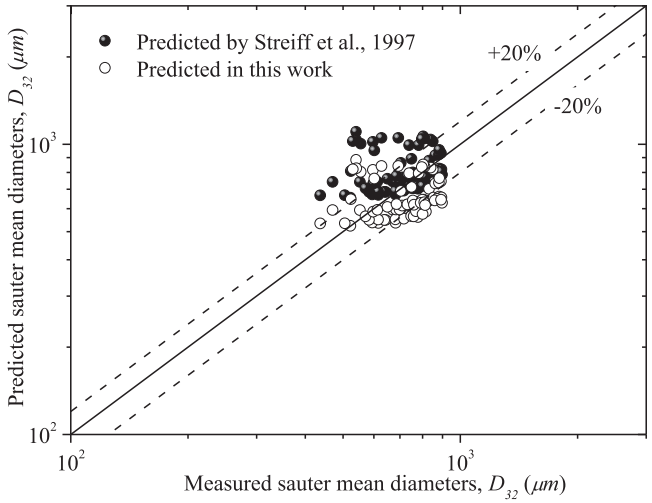

Fig. 11. Comparison between Streiff et al.'s model and model proposed in this work for d_{32} prediction.

CMC solution-gas flows.

$$\frac{d_{\max}}{D} = 0.33\left(\frac{\rho_c u_c^2 D}{\sigma}\right)^{-0.6} f^{-0.4} \tag{15}$$

D_{32} is another important parameter characterizing bubble size distribution. A number of models have been developed to predict the Sauter mean diameter from several dimensionless parameters. Streiff et al. (1997) and Zhang and Xu (2016) proposed Eq. (16) below to estimate the Sauter mean diameter of the oil drop in the transient and turbulent flow regimes.

$$\frac{d_{32}}{D_h} = 0.21We^{-0.5}Re_h^{0.15} \tag{16}$$

here the hydraulic Reynolds number Re_h can be obtained from Eq. (17), in which μ_m is the mixture viscosity. The Weber number We_h can be determined from Eq. (18) by taking into account the fluid mixture properties, hydraulic diameter, and interstitial velocity.

$$Re_h = \frac{\rho_m u_m D_h}{\alpha \mu_m} \tag{17}$$

$$We_h = \frac{\rho_m u_m^2 D_h}{\sigma \alpha^2}. \tag{18}$$

However, Streiff et al.'s model is not suitable for gas–liquid dispersions. In order to predict the Sauter mean diameter for a bubble, its modified version is proposed in this study (see Eq. (19)). A comparison of the prediction results obtained using Streiff et al.'s model and modification in this work is displayed in Fig. 11. The latter exhibits much better performance as compared to that of Streiff et al.'s model with a relative error of ±20%.

$$\frac{d_{32}}{D_h} = 0.15We^{-0.5}Re_h^{0.15}. \tag{19}$$

4.2. Validation of numerical simulations

Numerical simulations provide a detailed description of the fluid domain. In order to validate the reliability of the simulations, they must be conducted at the experimental operating conditions.

Fig. 12 shows a comparison between the simulation and experimental results in the form of a phase distribution contour. In this figure, the longitudinal phase distribution is compared with the photo of the gas core, while the cross-sectional phase distribution is compared with the contour of the ERT measurements. The blue color denotes the lowest values of the local void fraction α, while the red color represents its highest magnitudes (the other colors are used to designate the intermediate values). According to the longitudinal phase distribution contour, the gas phase accumulates in the pipe center, which matches the gas core in the experimental observations. The relatively wide region of the high values of the local void fraction results from the refraction of the pipe wall that makes the gas core visually thinner. In addition, the existence of the gas core is also confirmed by the local void fraction distribution obtained via numerical simulations and results of ERT measurements. After considering the distribution of local void fraction α at the location of the horizontal center line of the ERT sampling section in Fig. 13, it can be seen that its total trend (including the gas core) and amplitude are in good agreement with the ERT data. The minor discrepancy observed for the width of the gas core results from the pixel size of the ERT contour, which lowers the phase gradient during the rapid phase transition between the gas and the liquid. When integrating the radical distribution curve corresponding in Fig. 13, it can be seen that under 18 m^3/h inlet flow rates, the numerical curve integration is 1.89% and the ERT integration 2.85%. As with 16 m^3/h case, the numerical curve integration is 2.24% and the ERT integration 3.49%. The variation between numerical simulation and ERT measurement is acceptable. In general, the numerical simulation procedure used for the gas–liquid dispersion in this work is relatively reliable and can be utilized in future studies.

4.3. Phase distribution in a swirling flow field

4.3.1. Phase distributions at low inlet flow rates

Phase distributions at inlet flow rates lower than 18 m^3/h are mainly investigated by conducting flow experiments. In the swirling flow field, the gas phase is transferred to the pipe center and accumulates there in the form of a gas core, as shown in Fig. 14. This figure contains the photographs of the observation tube and ERT local void fraction contour obtained for three different inlet void fraction ε at inlet flow rates below 18 m^3/h. The maximal local void fraction is equal to 100% for all contours, indicating that the gas core contains a continuous gas phase, and its vicinity is depicted by a transitional color. It should be noted that the core region is larger in the void fraction contour than in the photograph (the same trend is observed for the transitional region), which results from the larger pixel resolution of the ERT electrode as compared with that of the interface between the gas core and the liquid. After taking into account the refraction of the Plexiglass tube (which visually narrows the gas core), the gas core size measured by ERT is slightly larger than that depicted in the photograph. However, this phenomenon has little effect on the ERT measurements of the local void fraction of the testing section.

Varying the inlet void fraction ε at a fixed inlet flow rate has very little effect on the size of the gas core and phase distribution in the swirling flow field. As shown in Fig. 15, at an inlet flow rate of the gas–pure water mixture equal to 16 m^3/h, the inlet void fraction ε changes from 12.0% to 26.7%, while the gas core size and distribution of the local void fraction α does not significantly vary in the downstream vane zone. To further investigate this phenomenon, the local void fraction distributions along the pipe horizontal center line obtained at different values of the inlet void fraction ε are plotted in Fig. 16 (the latter also contains the error bars for the ERT measurement data). It shows that the local void distribution curves nearly overlap with each other despite the changes in the inlet void fraction ε at a constant inlet flow rate. After integrating the local void fraction at the sampling section face, the phenomenon becomes more apparent. As shown in Fig. 17, little variations are observed at different inlet void fractions ε under the experimental operating conditions. Moreover, as the inlet flow

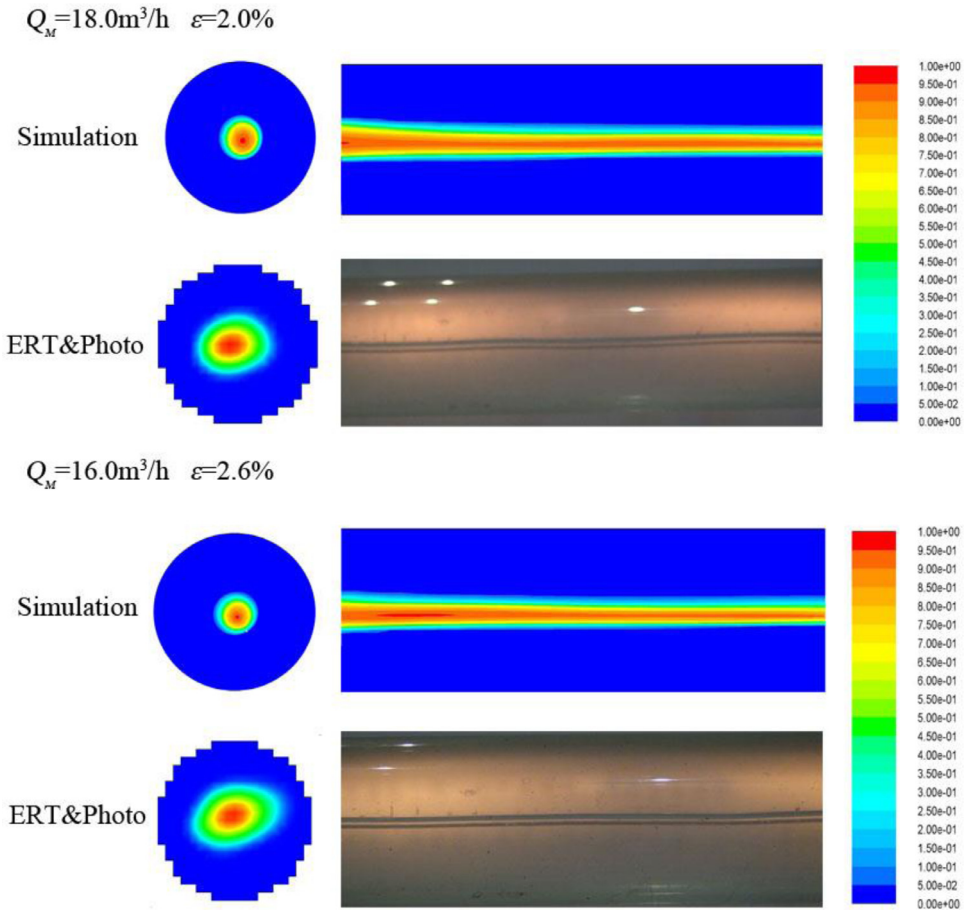

Fig. 12. Comparison of local void fraction between numerical simulation and experimental observation. (For interpretation of the references to color in this figure legend, the reader is referred to the web version of this article.)

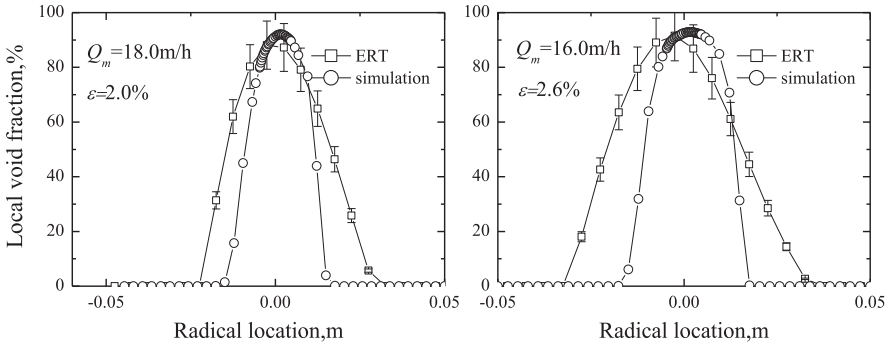

Fig. 13. Comparison of cross sectional void fraction distribution at location of horizontal center line for numerical simulation and ERT measurement.

rate increases, the total facial cross-sectional local void fraction increases as well, which can be attributed to the effect produced by the slip velocity between the gas and the liquid phases. Without consideration of slip velocity, the section void fraction would increase with inlet void fraction augment. The slip velocity promotes gas phase flow through liquid phase faster and increasing of slip velocity help section void fraction keep balanced. The resulting dynamic balance changes the fraction of the cross-section phase very little during the variation of the inlet flow rate from 5% to 30%.

4.3.2. Phase distributions at high inlet flow rates

The investigation of the phase distributions at high inlet flow rates are conducted mainly through numerical simulations. In this work, the high inlet flow rates are defined as those exceeding 18 m^3/h.

Figs. 18 and 19 display the longitudinal distributions of the local void fraction α determined at inlet flow rates of 56 m^3/h and 141 m^3/h after 10.0 and 4.0 s, respectively, and various inlet void fractions ε. The obtained results confirm the existence of a steady gas core in the swirling flow field. Moreover, the gas core size increases gradually at a constant inlet flow rate, which is different from the results obtained at low inlet flow rates. Fig. 20 shows the radial distribution of the local void fraction α determined at the operating conditions described in Figs. 18 and 19. The location of the section after the vane zone is 7.2*D*, which results from the narrowing of the gas core at relatively low slip velocities corresponding to the high inlet flow rates. In addition, the length of the

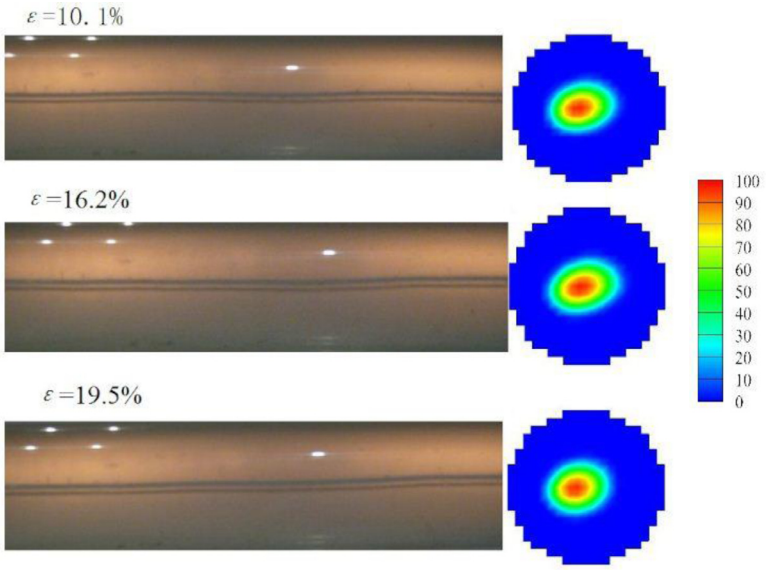

Fig. 14. Gas core configuration and cross section local void fraction distribution measured by ERT for gas–pure water flow under 18 m^3/h mixture inlet flow rate.

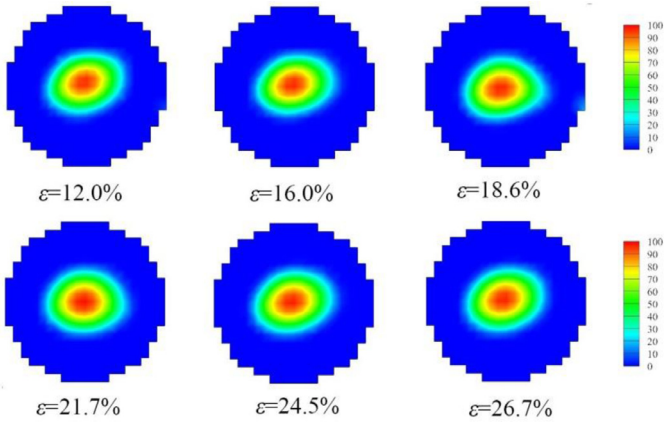

Fig. 15. Local void fraction of gas–pure water flow under 16 m^3/h mixture inlet flow rates.

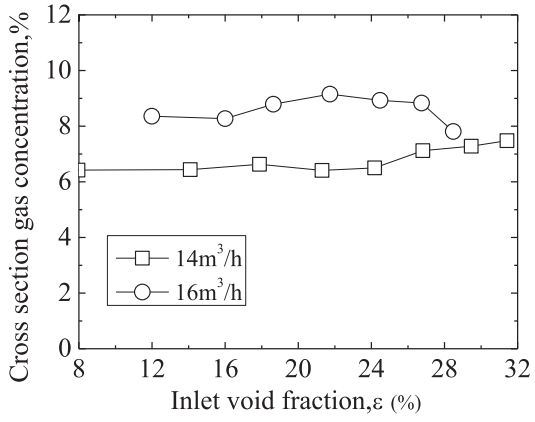

Fig. 17. Cross section void fraction integration of gas–pure water flow with various inlet void fractions.

developing section increases with an increase in the inlet void fraction ε, owing to the reduction in the swirling intensity by the high values of the inlet void fraction, which impede the convergence of the gas phase. As a result, more space is required to overcome this effect and converge the gas phase into a steady core. Moreover, increasing the inlet flow rate at a constant inlet void fraction decreases the time required by the core to reach stability and length of the development period. This phenomenon can be attributed to the higher tangential velocity that promotes the transfer of the gas phase to the pipe center at shorter distances.

Another important phenomenon is the shape of the gas core. As shown in Fig. 20, the local void fraction maintains the value of 100%, at a width radically different from that observed at low inlet flow rates (this phenomenon is more distinct at an inlet flow rate

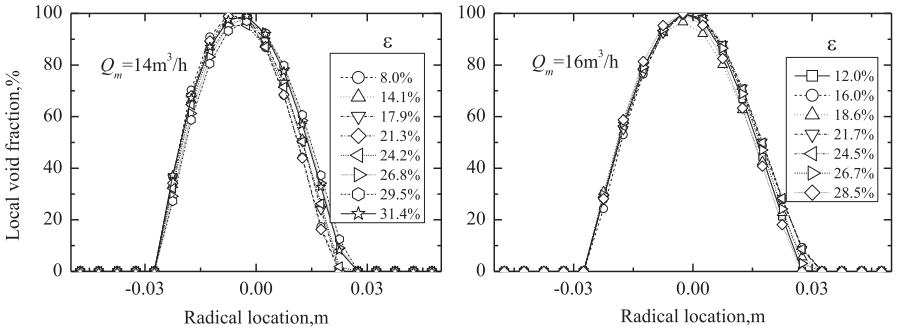

Fig. 16. Cross sectional local void fraction distribution at location of horizontal centerline of ERT electrode for 14 m^3/h and 16 m^3/h mixture inlet flow rate.

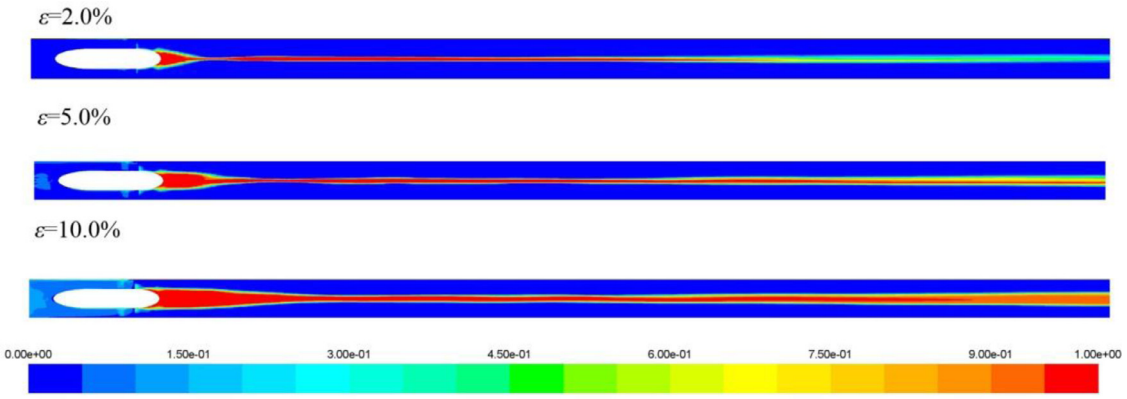

Fig. 18. Longitudinal local void fraction distribution for various inlet void fractions under 51 m^3/h mixing inlet flow rate at 10.0 s.

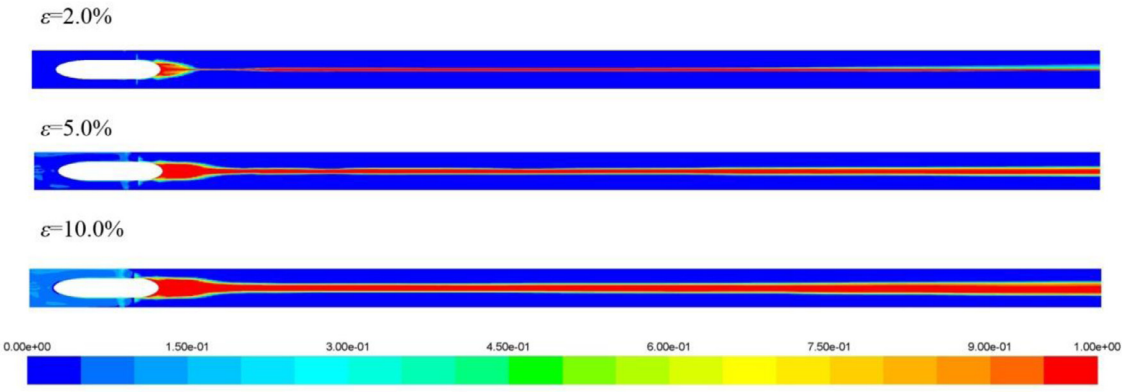

Fig. 19. Longitudinal local void fraction distribution for various inlet void fractions under 141 m^3/h mixture inlet flow rate at 4.0 s.

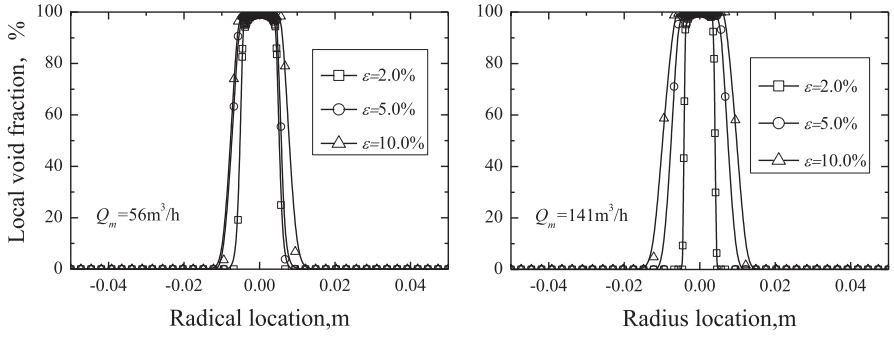

Fig. 20. Void fraction distribution at central line of ERT electrode for various inlet void fractions under 56 and 141 m^3/h mixture inlet flow rate.

of 141 m^3/h than at 56 m^3/h). Moreover, better convergence of the gas core is observed at an inlet flow rate of 141 m^3/h, which can be attributed to the higher tangential velocity that strongly promotes the phase transfer process in the radial direction.

4.3.3. Effects of liquid viscosity on gas distribution in the flow field

The purpose of the gas-CMC solution flow experiment is to investigate the effects produced by the liquid viscosity on the gas distribution in the flow field. Fig. 21 displays the variations in the inlet bubble distribution parameter d_{32} with the CMC concentration at an inlet flow rate of 16 m^3/h. It shows that the value of d_{32} increases with increasing inlet void fraction. Moreover, at a fixed inlet flow rate, d_{32} decreases with an increase in the CMC concentration for inlet void fraction between 7%–23%. According to Eqs. (17)–(19), the viscosity of the continuous phase increases with increasing CMC concentration, which minimizes the magnitude of

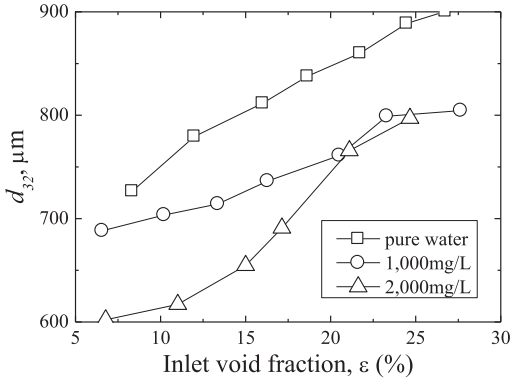

Fig. 21. Variation of d_{32} according to CMC concentration under 16 m^3/h mixture inlet flow rate.

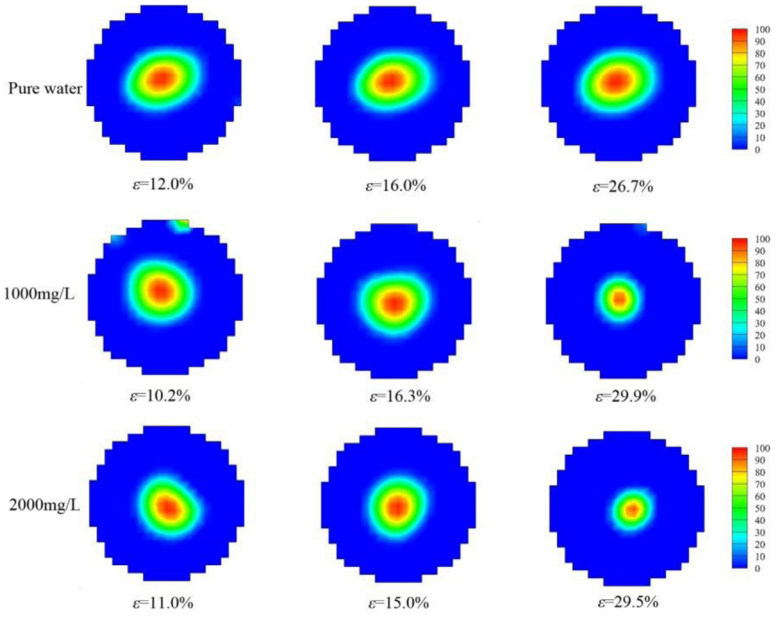

Fig. 22. Cross section local void fraction distribution for various CMC concentrations under 16 m^3/h mixture inlet flow rate measure by ERT.

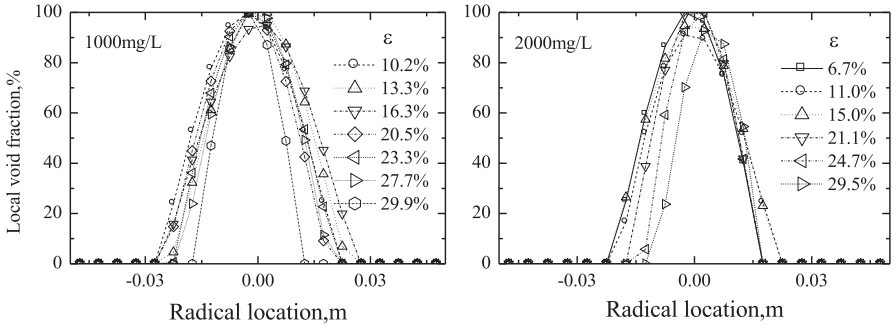

Fig. 23. Cross section local void fraction distribution at horizontal centerline of ERT electrode for gas-CMC solution flows under 16 m^3/h mixture inlet flow rate.

Re_h. In addition, the surface tension σ decreases with an increase in the CMC concentration, which in turn increases We_h. As a result, the value of d_{32} decreases, thus producing smaller bubbles at high CMC concentrations.

The CMC concentration also affects the gas core size. The results of the experimental observations and ERT local void fraction data presented in Figs. 22 and 23 exhibit two prominent trends. First, at a constant value of the inlet void fraction ε, the gas core size decreases with increasing CMC concentration rise, as shown in Fig. 22. The second trend shows that at a fixed inlet flow rate, the size of the gas core is sensitive to the inlet void fraction ε in the gas-CMC solution flow, which is different from the gas core in the gas–pure water flow. According to Fig. 23, as the inlet void fraction ε increases, the gas core gradually shrinks. After integrating the cross-sections of the local void fractions, this phenomenon becomes more pronounced, especially for the gas-CMC solution flows with inlet void fractions ε higher than 20%, as shown in Fig. 24. Theoretically, in addition to the effect produced by the inlet void fraction on the inlet bubble size, the properties of the continuous phase (such as viscosity) and swirling flow field may change as well. The higher gas–liquid viscosity increases the slip velocity, which results in a faster flow of the gas phase through the liquid phase, thus reducing the cross-sectional local void fraction. The latter in turn increases the concentration of the liquid phase, which enhances the swirling flow field and promotes the convergence of the gas core. This phenomenon is observed more distinctly at higher inlet void fractions due to compressibility of gas phase. Although smaller bubble sizes may increase the size of the gas core, their influence is negligible compared with the tremendous gas–liquid density difference and effect produced by the gas–liquid surface tension and viscosity.

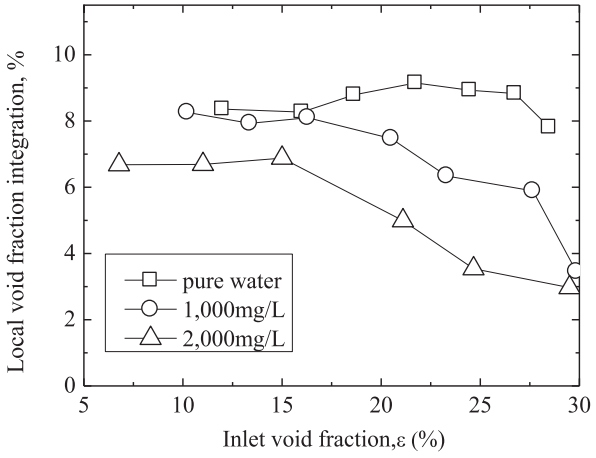

Fig. 24. Cross section void fraction integration for various CMC concentrations.

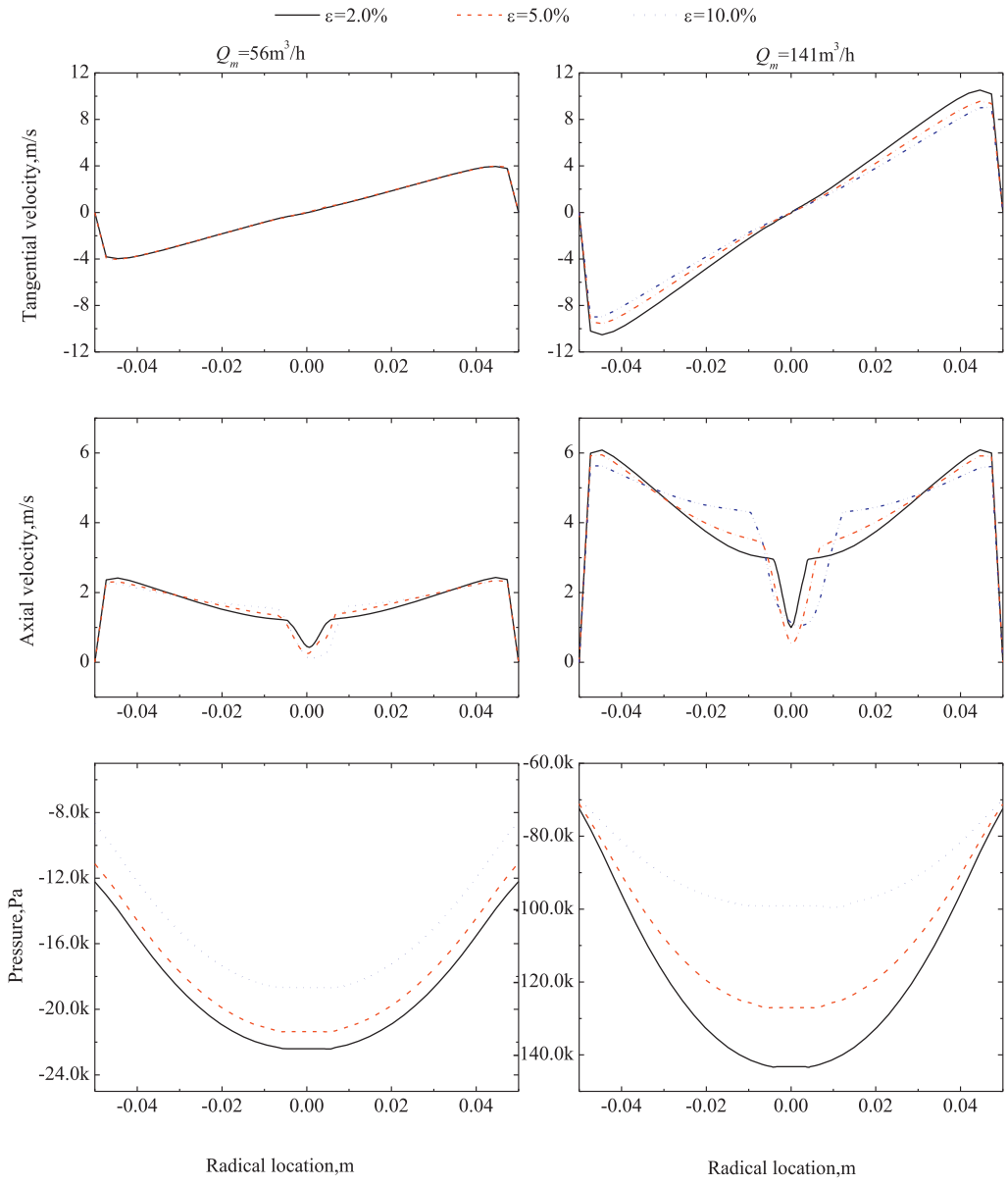

Fig. 25. Pressure and velocity distribution for cross sections 7.2D downstream vane zone for various inlet void fractions under 56 and 141 m^3/h mixture inlet flow rates.

4.4. Continuous phase studies

4.4.1. Influence of gas phase on velocity and pressure distribution

Fig. 25 describes the radial velocity and pressure distributions in the 7.2*D* downstream vane zone. The inlet flow rates are equal to 56 and 141 m^3/h, while the inlet void fraction ε varies from 2.0% to 10.0%. From the obtained results, it can be concluded that the velocity and pressure distributions exhibit similar trends at different inlet flow rates with some discrepancies in the amplitude. For the tangential velocity distributions, a monotonous curve from the pipe center to the inner wall is obtained with zero values at both its endpoints. At an inlet flow rate of 56 m^3/h, the influence of the gas phase is negligible. However, as its value increases to 141 m^3/h, the presence of the gas phase reduces the velocity amplitude. The higher inlet void fractions also lower the velocity amplitude. For the axial velocity distributions, the influence of the inlet void fraction is negligible at an inlet mixture flow rate of 56 m^3/h and more considerable at 141 m^3/h. The higher inlet void fraction results in higher axial velocity near gas core while reduces axial velocity near swirling flow field boundary. In the pipe center, the gas phase is the continuous phase, local water holdup is low in the gas core and phase transition part. As a consequence, an abrupt valley of water phase velocity appears at the pipe center corresponding to size of gas core.

Increasing the inlet void fraction results in a mild pressure drop from the inner wall to the pipe center. Here, it should be noted that in cases with high mixture inlet flow rates, without experimental data on the pressure information, outflow boundary conditions are applied, with center of inlet vane section as reference point. The pressure in the figure is a relative value to operating conditions. When taken consideration of operating pressure together, the pressure is positive. Similar to the tangential and axial velocities, the influence of the inlet void fraction on the pressure distribution is stronger at high inlet flow rates. Theoretically, increasing the inlet flow rate promotes centrifugal acceleration, which leads to a steeper pressure distribution of the radial velocity amplitude. As a result, the bubbles flowing from the vane zone are transported faster at higher collision and coalescence frequen-

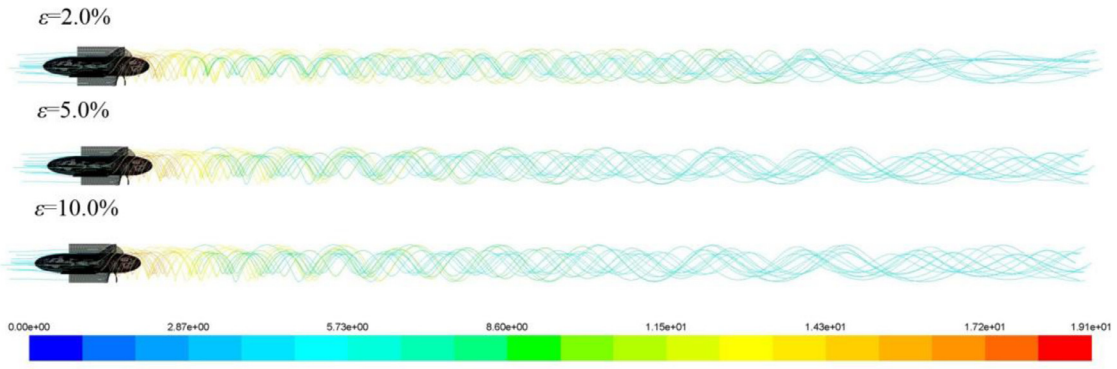

Fig. 26. Streamline distribution for various inlet void fractions under 141 m^3/h mixture inlet flow rate at 4.0 s.

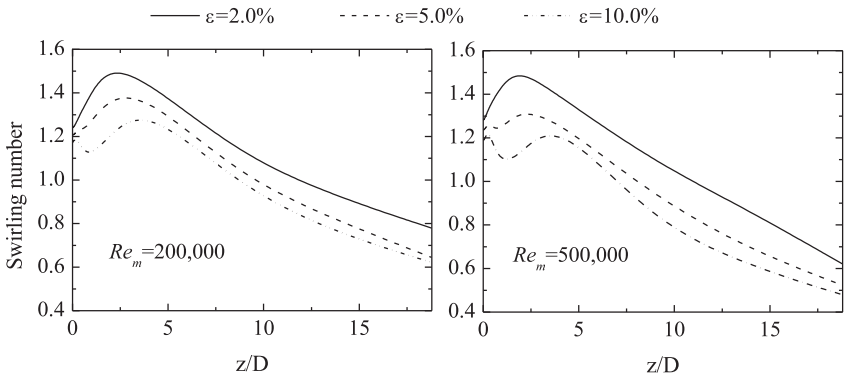

Fig. 27. Swirling number distribution along the pipe for various inlet void fractions under different mixture inlet Reynolds number.

cies. All these factors make the influences of the inlet void fraction more obvious.

4.4.2. Intensity of the gas–liquid swirling flow field

Fig. 26 shows the streamlines obtained at various inlet void fractions ε and inlet flow rate of 141 m^3/h after 4.0 s. Their shapes apparently become twisted and rotated in the vane zone. From the twisting angle, the magnitude of the swirling intensity can be estimated with certain accuracy. In the literature (Walstra, 1993; Ahmed et al., 2015; You and Zhou, 2006), the swirling intensity is typically quantified by the swirling number Ω, which is defined as the ratio of the tangential momentum to the axial flux of the axial momentum:

$$\Omega=\frac{1}{R_2}\frac{\int_{R_1}^{R_2} r^2 v_t v_x dr}{\int_{R_1}^{R_2} r v_x^2 dr} \tag{20}$$

where R_2 is the outer radius of the cross-section, R_1 is the inner radius of the cross-section, and v_t and v_x are the tangential and axial velocities of the mixture, respectively.

Using the swirling number, the influence of inlet void fraction on swirling intensity at various inlet velocities can be determined. Fig. 27 displays the variations of the axial swirling number with the inlet void fraction ε and Reynolds number Re_m. Here, the axial distance is normalized with respect to the inner diameter D, and its zero value represents the section beginning immediately after the vane zone. Clearly, the swirling number increases to a maximal value at a short distance after the vane zone and then gradually decreases. At all the studied Re_m values, the presence of the gas phase decreases the swirling number. Moreover, at high inlet void fractions, the curvature of the swirling number exhibits a decrease right after the vane zone and then increases to a maximum

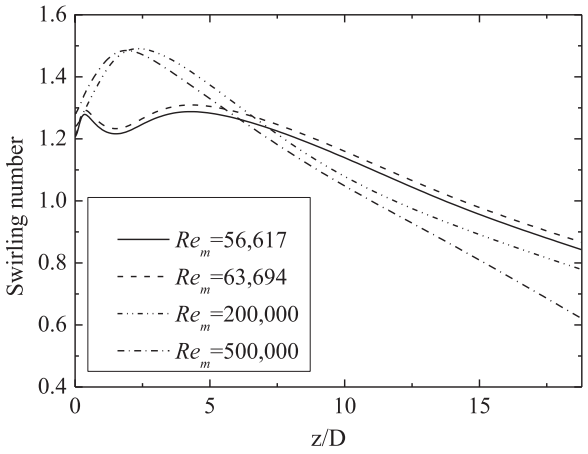

Fig. 28. Swirling number distribution along the pipe for fixed inlet void fraction (2%) under various inlet mixture Reynolds number.

value. Here, the described section corresponds to the developing sections in Figs. 18 and 19. The phenomenon can be explained as follows: the gas phase in the pipe center has a lower density. As the slip velocity between the phases decreases, the swirling intensity and continuity of the liquid phase are reduced. In addition, the decrease in the swirling number observed in the developing part of the flow domain, where the local void fraction is relatively large, becomes more apparent.

The variations of the swirling number with Re_m determined at a constant inlet void fraction are shown in Fig. 28. Here, the axial distance is normalized with respect to the pipe diameter D as well. The swirling numbers obtained at high inlet flow rates

and Re_m values larger than 64,000 have higher amplitudes than those obtained at lower flow rates cases before 7*D*, while the latter magnitudes decrease slower than the former ones. This is because under high inlet Re_m conditions, the inertial of fluids induces stronger swirling intensity and makes turbulent dissipation more severe than Re_m lower than 64,000, as a consequence, the swirling number attenuate more rapidly and falls lower than low Re_m conditions in the swirling flow field. Furthermore, the influence of the developing section on the swirling number is observed at lower inlet flow rates as well because the bubbles in this case require more space to converge into a core.

5. Conclusion

In this work, both flow loop experiments and numerical studies are conducted to investigate bubble size and gas phase distributions in a swirling flow field. The flow loop experiments utilize the Malvern RTsizer and EIT 3000 instruments to measure the inlet bubble size and local void fraction distributions, respectively, while the numerical studies combine the RNG k-ε turbulent model and the mixture multiphase model to determine the local void fractions and swirling intensities. From the obtained results, the following conclusions can be drawn:

The prediction model for the maximal drop diameter originally proposed by Hinze in 1955 is modified by varying its constant parameter to make it applicable under the utilized flow loop experimental conditions. Moreover, Streiff et al.'s model predicting drop d_{32} is also developed to describe bubble d_{32}, which shows better performance compared with the original model.

At low inlet flow rates corresponding to the experimental conditions, the obtained inlet void fractions ranging from 5% to 30% have little effect on the size of the gas core. The presence of CMC, which changes the interfacial tension and viscosity of the liquid phase, reduces the integral cross-sectional void fraction and narrows the gas core. At higher inlet flow rates (greater than 51 m^3/h), the size of the gas core increases with increasing inlet void fraction and becomes more converged.

The influence of the gas phase on the velocity and pressure distribution in the swirling flow field is stronger at higher inlet flow rates, and the same trend is observed for the swirling number. Increasing the inlet void fraction lowers the magnitude of the swirling number at a constant inlet flow rate. The swirling numbers corresponding to higher inlet flow rates exhibit larger amplitudes and decrease faster as compared to those of the swirling numbers obtained at lower inlet flow rates. The findings of this study lead to a better understanding of the bubble size and gas phase distributions in a vane-type swirling flow field and, therefore, can be used for designing separators in the oil extraction industry.

Acknowledgments

The authors gratefully acknowledge that the work described here is financially supported by National Natural Science Foundation of China (no. 51779243) and the Strategic Priority Research Program of the Chinese Academy of Science (grant no: XDB22030101).

Supplementary materials

Supplementary material associated with this article can be found, in the online version, at doi:10.1016/j.ijmultiphaseflow.2018.05.025.

References

Ahmed, Z.U., Al-Abdeli, Y.M., Guzzomi, F.G., 2015. Impingement pressure characteristics of swirling and non-swirling turbulent jets. Exp. Therm. Fluid Sci. 68, 722–732.
Brennan, M., 2016. CFD simulations of hydrocyclones with an air core-comparison between large eddy simulations and a second moment closure. Chem. Eng. Res. Des. 84, 495–505.
Cai, B., Wang, J., Sun, L., Zhang, N., Yan, C., 2014. Experimental study and numerical optimization on a vane-type separator for bubble separation in tmsr. Prog. Nucl. Energy. 74, 1–13.
Escue, A., Cui, J., 2010. Comparison of turbulence models in simulating swirling pipe flows. Appl. Math. Modell. 34, 2840–2849.
Funahashi, H., Hayashi, K., Hosokawa, S., Tomiyama, A., 2016. Study on two-phase swirling flows in a gas–liquid separator with three pick-off rings. Nucl. Eng. Des. 308, 205–213.
Hinze, J.O., 1955. Fundamentals of the hydrodynamic mechanism of splitting in dispersion processes. AICHE J. 1, 289–295.
Hirleman, E.D., Oechsle, V., Chigier, N.A., 1984. Response characteristics of laser diffraction particle size analyzers: optical sample volume extent and lens effects. Opt. Eng. 23, 610–619.
Hoffmann, A.C., Peng, W., Dries, H., Regelink, M., Foo, K., 2006. Effect of pressure recovery vanes on the performance of a swirl tube, with emphasis on the flow pattern and separation efficiency. Energy Fuels 20, 1691–1697.
Hreiz, R., Lainé, R., Wu, J., Lemaitre, C., Funfschilling, D., 2014. On the effect of the nozzle design on the performances of gas-liquid cylindrical cyclone separators. Int. J. Multiphase Flow. 58, 15–26.
Javadi, A., Bosioc, A., Nilsson, H., Muntean, S., Susan-Resiga, R., 2016. Experimental and numerical investigation of the precessing helical vortex in a conical diffuser, with rotor-stator interaction. Fluid. Eng. J. 138, 081106.
Jawarneh, A.M., Tlilan, H., Al-Shyyab, A., Ababneh, A., 2008. Strongly swirling flows in a cylindrical separator. Miner. Eng. 21 (5), 366–372.
Klujszo, L.A.C., Songfack, P.K., Rafaelof, M., Rajamani, R.K., 1999. Design of a stationary guide vane swirl air cleaner. Miner. Eng. 12, 1375–1392.
Liu, S., Zhang, D., Yang, L., Xu, J., 2018. Breakup and coalescence regularity of non-dilute oil drops in a vane-type swirling flow field. Chem. Eng. Res. Des. 129, 35–54.
Rafee, R., Rahimzadeh, H., 2010. Performance evaluation of a curved type vane separator at different plate spacing in the range of 25 to 35 mm using numerical simulation. Iranian J. Chem. Chem. Eng. 29, 95–108.
Saidi, M., Maddahian, R., Farhanieh, B., 2013. Numerical investigation of cone angle effect on the flow field and separation efficiency of deoiling hydrocyclones. Heat Mass Transf. 49, 247–260.
Shi, S.Y., Xu, J.Y., 2015. Flow field of continuous phase in a vane-type pipe oil–water separator. Exp. Therm. Fluid Sci. 60, 208–212.
Streiff, F.A., Mathys, P., Fisher, T.U., 1997. New fundamentals for liquid-liquid dispersion using static mixers. Rec. Progr. Genie Proc. 11, 307–314.
Walstra, P., 1993. Principles of emulsion formation. Chem. Eng. Sci. 48, 333–349.
Wang, A., Marashdeh, Q., Fan, L.S., 2016. ECVT imaging and model analysis of the liquid distribution inside a horizontally installed passive cyclonic gas–liquid separator. Chem. Eng. Sci. 141, 231–239.
Wang, M., Mann, R., Dickin, F., 1999. Electrical resistance tomographic sensing systems for industrial applications. Chem. Eng. Commun. 175, 49–70.
Yin, J.L., Li, J.J., Ma, Y.F., Wang, D.Z., 2017a. Numerical approach on the performance prediction of a gas-liquid separator for TMSR. Nucl. Sci. Tech. J. 8, 1–8.
Yin, J., Qian, Y., Ma, Y., Wang, D., 2017b. Experimental study on the bubble trajectory in an axial gas-liquid separator applied for tritium removal for molten salt reactors. Nucl. Eng. Des. 320, 133–140.
You, C., Zhou, Y., 2006. Effect of operation parameters on the slagging near swirl coal burner throat. Energy Fuels 20, 1855–1861.
Zhang, J., Xu, J., 2016. Rheological behavior of oil and water emulsions and their flow characterization in horizontal pipes. Can. J. Chem. Eng. 94, 324–331.